

Current-induced spin polarization in monolayer InSe

Ma Zhou ^{1,2,3}, Shengbin Yu,^{1,2} Wen Yang,⁴ Wen-kai Lou ^{1,2}, Fang Cheng,⁵ Dong Zhang,^{1,2} and Kai Chang^{1,2,3,*}

¹SKLSM, Institute of Semiconductors, Chinese Academy of Sciences, P.O. Box 912, Beijing 100083, China

²CAS Center for Excellence in Topological Quantum Computation, University of Chinese Academy of Sciences, Beijing 100190, China

³Beijing Academy of Quantum Information Sciences, Beijing 100193, China

⁴Beijing Computational Science Research Center, Beijing 100193, China

⁵Department of Physics and Electronic Science, Changsha University of Science and Technology, Changsha 410004, China



(Received 2 November 2019; published 11 December 2019)

We find that perpendicular electric fields can give rise to a tunable current-induced spin polarization in monolayer InSe. The interplay between the Rashba and the intrinsic Dresselhaus spin-orbit coupling leads to several Lifshitz transitions near the valence band maxima. Interestingly, the sign of the spin polarization changes with increasing perpendicular electric fields. We propose a spin potentiometric device to measure current-induced spin polarization.

DOI: [10.1103/PhysRevB.100.245409](https://doi.org/10.1103/PhysRevB.100.245409)

I. INTRODUCTION

Layered III-VI semiconductors such as InSe and GaSe are well known for their intrinsic outstanding properties and potential applications in nonlinear optics. Recently, their two-dimensional (2D) counterparts also attracted much attention as the next generation of graphenelike materials. First-principles calculations [1–5] reveal an unusual nonparabolic topmost valence band (called the Mexican hat) with a large density of states (DOS) and van Hove singularity at the top of the valence band when the sample thickness is less than six layers. The recent experimental growth of few-layer GaSe and InSe [6,7] further aroused great enthusiasm for these materials [4,8].

The current-induced spin polarization (CISP), also known as the Edelstein effect [9] or the charge-to-spin conversion [10,11], is that a charge current driven through a 2D system with Rashba spin-orbit coupling (RSOC) generates a spatially homogeneous spin polarization perpendicular to the applied bias. Thus a nonzero spin polarization is generated in nonmagnetic systems purely electrically. The RSOC induced by the structural inversion asymmetry or perpendicular electric field (PEF) is responsible for CISP taking place in interfaces and 2D materials, where the RSOC can be tuned by gate voltages [12]. Recent experiments have demonstrated that a charge current produces a net spin polarization in both Bi₂Se₃ films and conventional two-dimensional electron gas (2DEGs) formed at InAs(001) [13,14]. Surprisingly, these spin polarizations induced by charge current can directly be manifested as a voltage on a ferromagnetic contact.

Although the CISP is induced by the RSOC, it can also be tuned by the Dresselhaus spin-orbit coupling (DSOC). In 2007, Maxim investigated the CISP in the two-dimensional electron gases with both the Rashba and Dresselhaus spin-orbit couplings using an exact solution of the Boltzmann

equation [15]. He finds that the spin response to an in-plane electric field turns out to be highly anisotropic. Using the same model Hamiltonian, Mathias finds that the CISP disappears when the Rashba and Dresselhaus SOC have the same strengths [16]. All these works are common in that they study the CISP in 2DEGs with C_{2v} symmetry as determined by the Hamiltonian near the Γ point and take both the RSOC and DSOC effects into consideration. In recent years, the successful fabrication of graphene and TMDC have aroused enthusiasm for studying the CISP in 2D materials with C_3 symmetry [17–19]. However, the band dispersion near the Fermi energy is around the K point in the Brillouin zone.

Here, we study the CISP in monolayer InSe and the spin response was determined by the energy dispersion around Γ point with C_3 symmetry. Since the monolayer InSe has spatial inversion asymmetry, it possesses a large intrinsic Dresselhaus spin-orbit coupling effect [20]. The interplay between the gate voltage induced RSOC and the intrinsic DSOC near the topmost of the valence band leads to several Lifshitz transitions with increasing the RSOC. The Lifshitz transition leads to a sign change of the spin polarization when the chemical potential μ lies very close to the valence band maxima. Therefore, observing this phenomenon only requires a small doping density and should be experimentally accessible. This phenomenon also offers us a new way to manipulate the direction of the in-plane spin polarization by tuning the PEF. Since the spin polarization is a central issue in spintronics [10,11,19,21–23], the CISP sign change in monolayer InSe may be used to construct extremely thin spintronic devices.

The rest of this paper is organized as follows. In Sec. II, we add the RSOC and DSOC terms into the 14-band $\mathbf{k} \cdot \mathbf{p}$ Hamiltonian [8] by analyzing the crystal symmetry. In Sec. III A, we calculate the charge-to-spin conversion of the monolayer InSe under different Rashba coefficients based on our $\mathbf{k} \cdot \mathbf{p}$ model. In this section, we also establish a relationship between the value of Rashba coefficients with the magnitude of the PEF. By using the tight-binding model, we calculate the charge-to-spin conversion under different PEF magnitudes

*Corresponding author: kchang@semi.ac.cn

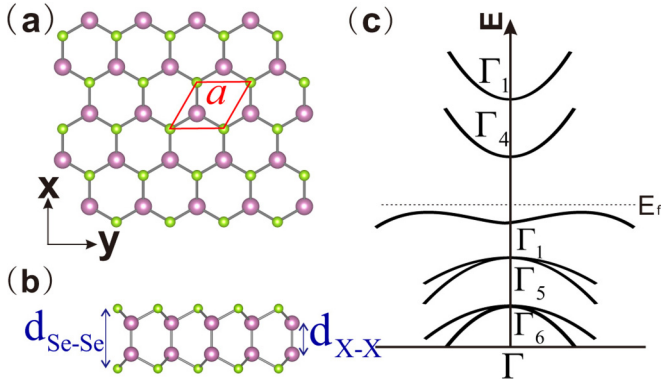


FIG. 1. Crystal structure of monolayer InSe shown in (a) top view and (b) side view. (c) Sketch of the monolayer InSe electronic bands around the Γ point, omitting the spin-orbit coupling.

$$\mathbf{H}_0 = \begin{bmatrix} Gk^2 & 0 & 0 & ib_{54}^{vc}k_x & ib_{54}^{vc}k_y & 0 & 0 \\ & Fk^2 & b_{11}^{vc}k^2 & 0 & 0 & ib_{61}^{vc}k_x & ib_{61}^{vc}k_y \\ & & Mk^2 & -i\lambda_{15}s_y & i\lambda_{15}s_x & ib_{61}^{vc}k_x & ib_{61}^{vc}k_y \\ & & & Ak^2 + B(k_y^2 - k_x^2) & -2Bk_xk_y - i\lambda_5s_z & 0 & 0 \\ & & & Ak^2 - B(k_y^2 - k_x^2) & Ak^2 - B(k_y^2 - k_x^2) & 0 & 0 \\ & & & & & Ck^2 + D(k_y^2 - k_x^2) & -2Dk_xk_y - i\lambda_6s_z \\ & & & & & & Ck^2 - D(k_y^2 - k_x^2) \end{bmatrix}. \quad (2)$$

Here, $k_x(k_y)$ is along $\Gamma \rightarrow M(\Gamma \rightarrow K)$ axis and we only keep the lowest order contribution to each matrix element. All the parameters in the Hamiltonian $\mathbf{H}_{\mathbf{k},\mathbf{p}}$ are obtained by fitting the first-principles calculations. Hamiltonian Eq. (1) can well describe the band dispersion around the Γ point in the presence of spin-orbit coupling. However, the Dresselhaus spin splitting along $\Gamma \rightarrow K$ direction cannot be reproduced by the Hamiltonian Eq. (1). The RSOC and DSOC can be described by adding the invariants $\alpha(k_x s_y - k_y s_x)$ and $\lambda_D(3k_x^2 k_y - k_y^3)s_z$, respectively, into the Hamiltonian as

$$\mathbf{H}_{\text{tot}} = \mathbf{H}_{\mathbf{k},\mathbf{p}} + \lambda_D(3k_x^2 k_y - k_y^3)s_z + \alpha(k_x s_y - k_y s_x). \quad (3)$$

Here, $\lambda_D = 0.2$ is obtained by comparing the spin splitting energy calculated by the Hamiltonian Eq. (3) with that obtained from first principles calculations along the $\Gamma \rightarrow K$ direction, as shown in Appendix A. The Rashba coefficients α can be tuned by increasing the magnitude of the PEF. By diagonalizing the Hamiltonian \mathbf{H}_{tot} without the PEF ($\alpha = 0$), we can obtain the band structure displayed in Figs. 2(a) and 2(b). As we can see, the energy bands are split (degenerate) along the $\Gamma \rightarrow K$ ($\Gamma \rightarrow M$) direction. This is different from the bilayer InSe band structure obtained in our former work, where the energy bands are split along both directions [20]. Since the bilayer InSe lacks mirror symmetry and has a built-in electric field induced by its *AB*-stacking structure, there is an *intrinsic* Rashba spin splitting along the $\Gamma \rightarrow M$ direction in bilayer InSe without external PEF. Compared with the bilayer InSe, the monolayer InSe does not have an *intrinsic* Rashba type spin splitting along the $\Gamma \rightarrow M$

by adding the on-site energy. In Sec. III B, we perform further calculations to take into account the disorder effect and obtain the charge-to-spin conductivity with different Rashba coefficients for different disorder strengths. The summary and final conclusions are in given Sec. IV.

II. MULTIBAND $\mathbf{k} \cdot \mathbf{p}$ HAMILTONIAN OF MONOLAYER METAL CHALCOGENIDE

As shown in Fig. 1, the unit cell of the monolayer InSe consists of four ions in two sublayers, with one indium and one selenium in each sublayer. By adopting the standard invariant theory [8], the $\mathbf{k} \cdot \mathbf{p}$ Hamiltonian for InSe monolayer with the D_{3h} point group incorporating the spin-orbit coupling effects can be written as

$$\mathbf{H}_{\mathbf{k},\mathbf{p}} = \text{diag}\{E_{c4}, E_{c1}, E_{v1}, E_{v5}, E_{v5}, E_{v6}, E_{v6}\} + \mathbf{H}_0, \quad (1)$$

where E_{c4}, \dots, E_{v6} are band-edge energies, and

direction. However, the Rashba spin splitting can be induced by adding external PEF on monolayer InSe. By increasing the Rashba coefficient from zero to a critical value, the spin splitting along the $\Gamma \rightarrow M$ increase from zero to a comparable

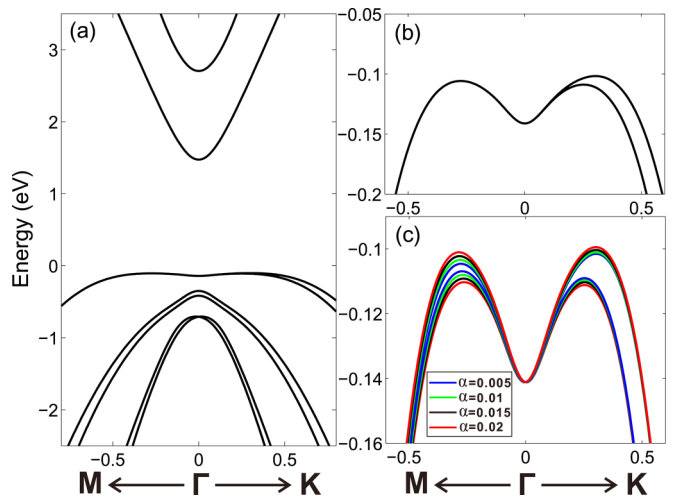


FIG. 2. (a) Energy band structure of monolayer InSe (with SOC) from our $\mathbf{k} \cdot \mathbf{p}$ model Hamiltonian \mathbf{H}_{tot} with $\alpha = 0$. (b) Detailed structure of the topmost valence band shown in (a). (c) Top-most valence band structure with different Rashba coefficients $\alpha = 0.005$ eV \AA (blue lines), $\alpha = 0.01$ eV \AA (green lines), $\alpha = 0.015$ eV \AA (black lines), and $\alpha = 0.02$ eV \AA (red lines).

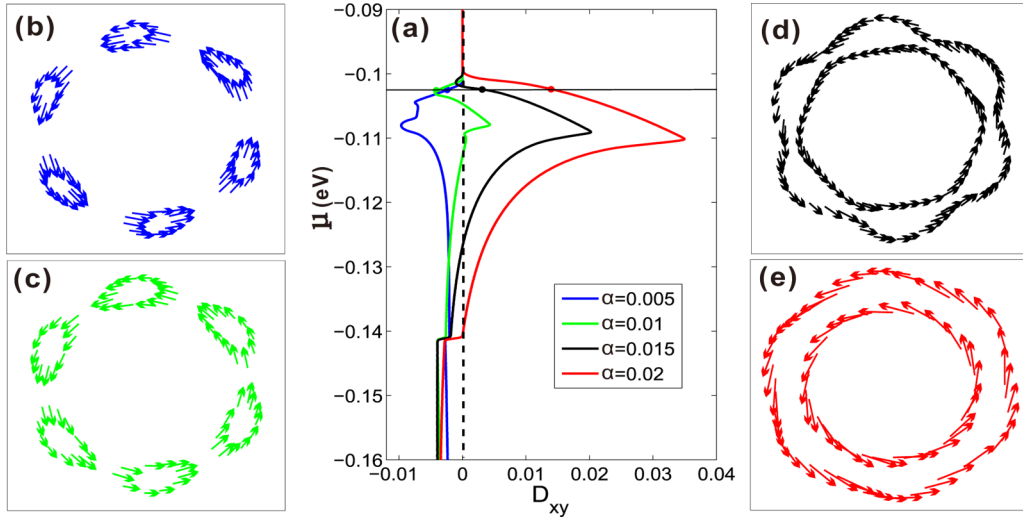


FIG. 3. (a) Charge-to-spin response D_{xy} of monolayer InSe in the clean limit ($\tau \rightarrow \infty$), from the multiband $\mathbf{k} \cdot \mathbf{p}$ model for different Rashba coefficients $\alpha = 0.005$ eV Å (blue line), $\alpha = 0.01$ eV Å (green line), $\alpha = 0.015$ eV Å (black line), and $\alpha = 0.02$ eV Å (red line). Panels (b)–(e) show the spin texture (arrows) at the Fermi circles at chemical potential $\mu_0 = -0.1025$ eV [black horizontal line in (a)] for different Rashba coefficients (b) $\alpha = 0.005$ eV Å, (c) $\alpha = 0.01$ eV Å, (d) $\alpha = 0.015$ eV Å, and (e) $\alpha = 0.02$ eV Å.

value with the splitting along the $\Gamma \rightarrow K$ direction, as shown by the red lines in Fig. 2(c).

III. CHARGE-TO-SPIN CONDUCTIVITY

According to the Onsager relation, the charge-to-spin conductivity (C-S conductivity) is equal to the spin-to-charge conductivity, which reads [24]

$$\sigma_{\alpha\beta}^{\text{SGE}} = -\frac{e}{2\pi} \int \frac{d^2p}{(2\pi)^2} \text{Tr}[J_\alpha G^R(\mu) s_\beta G^A(\mu)], \quad (4)$$

where $J_\alpha = ev_\alpha = e\partial\mathbf{H}_{\text{tot}}/\partial k_\alpha$ ($\alpha = x, y$) is the current operator, s_β is the spin operator, and $G^{R(A)}$ is the retarded (advanced) Green function corresponding to the unperturbed Hamiltonian \mathbf{H}_{tot} , taken at the chemical potential μ . For the clean-limit situation, the C-S conductivity $\sigma_{\alpha\beta}^{\text{SGE}}$ could become divergent. This would not happen in real materials, where the impurity scattering causes a finite lifetime of the carriers.

A. Clean-limit Drude coefficient

In the clean limit, the carrier lifetime $\tau \rightarrow \infty$ and the conductivity $\sigma_{\alpha\beta}^{\text{SGE}}$ diverge as $\sigma_{\alpha\beta}^{\text{SGE}} = D_{\alpha\beta}\tau$, where

$$D_{\alpha\beta} = -\text{Re} \int \frac{d^2\mathbf{k}}{2\pi} [f(E_{-\mathbf{k}}) - f(E_{+\mathbf{k}})] \frac{\langle -, \mathbf{k} | s_\alpha | +, \mathbf{k} \rangle \langle +, \mathbf{k} | J_\beta | -, \mathbf{k} \rangle}{E_{-\mathbf{k}} - E_{+\mathbf{k}} + i/(2\tau)}. \quad (5)$$

Here $f(E) = 1/(e^{(E-\mu)/(k_B T)} + 1)$ is the Fermi distribution, τ is the lifetime of the carriers ($\tau \rightarrow \infty$ for clean-limit system), $E_{+\mathbf{k}}$ ($E_{-\mathbf{k}}$) is the upper (lower) spin-split branch of the topmost valence band, and $|\pm, \mathbf{k}\rangle$ are the corresponding wave functions. The chemical potential μ can be tuned by gate voltages [25]. Only the Drude coefficients D_{xy} and D_{yx} are nonzero and they obey $D_{xy} = -D_{yx}$. At zero temperature, when $E_{-\mathbf{k}} < \mu < E_{+\mathbf{k}}$, the lower spin-split branch is

occupied, and the upper spin-split branch is empty, the charge-to-spin response D_{xy} near the valence band maxima has a negative/positive value for a relatively small/large Rashba coefficient $\alpha = 0.005$ eV Å, $\alpha = 0.02$ eV Å [see the blue and red lines in Fig. 3(a)]. It means that one can find the sign change in D_{xy} with increasing the perpendicular electric fields.

The sign change of D_{xy} can be understood as a consequence of the Lifshitz transition. At the chemical potential $\mu = \mu_0$ [the black horizontal line shown in Fig. 3(a)], the upper spin-split branch of the anisotropic topmost valence band gives rise to six small Fermi packets [the blue lines shown in Fig. 3(b)] for $\alpha = 0.005$ eV Å. The anisotropic spin splitting arises from the interplay between Rashba and Dresselhaus SOC. The six Fermi packets become larger when the Rashba coefficient increases to $\alpha = 0.01$ eV Å, as shown by the green line in Fig. 3(c). At the chemical potential $\mu = \mu_0$, the Drude coefficients D_{xy} are negative for both cases ($\alpha = 0.005$ eV Å and $\alpha = 0.01$ eV Å). However, the six Fermi packets merge into two big Fermi circles [as shown in Fig. 3(d)] when the Rashba coefficient increases to $\alpha = 0.015$ eV Å. This change can be understood as a Lifshitz transition induced by the perpendicular electric fields at certain chemical potential $\mu = \mu_0$ near the topmost of the valence band, i.e., the Mexican hat.

Next, we confirm the results above by utilizing the tight-binding model, which can also be used to evaluate the Rashba coefficients induced by different E_z strengths. By comparing the spin splitting energy along the $\Gamma \rightarrow M$ direction from the multiband $\mathbf{k} \cdot \mathbf{p}$ model with those from the tight-binding model shown in Appendix B, we obtain $\alpha = 0.4545E_z$. Therefore, the electric field strength corresponding to the Rashba coefficients shown in Fig. 3(a) are $E_z = 0.011$ V/Å ($\alpha = 0.005$ eV Å), $E_z = 0.022$ V/Å ($\alpha = 0.01$ eV Å), $E_z = 0.033$ V/Å ($\alpha = 0.015$ eV Å), and $E_z = 0.044$ V/Å ($\alpha = 0.02$ eV Å). As shown in Fig. 4(a), a significant sign change for the Drude coefficient D_{xy} can be obtained

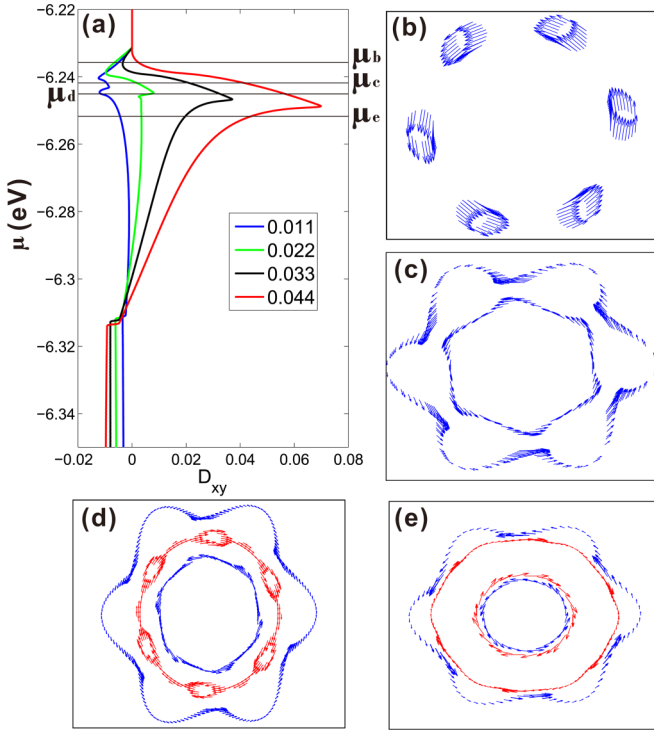


FIG. 4. (a) Charge-to-spin response D_{xy} of monolayer InSe in the clean limit ($\tau \rightarrow \infty$), from the tight-binding model for different perpendicular electric fields $E_z = 0.011$ V/Å (blue line), $E_z = 0.022$ V/Å (green line), $E_z = 0.033$ V/Å (black line), and $E_z = 0.044$ V/Å (red line). Panels (b)–(e) show the spin texture (arrows) on the Fermi circles at different chemical potentials $\mu = \mu_b, \mu_c, \mu_d, \mu_e$ [shown in (a)]: blue (red) lines for the upper (lower) spin-split branch of the topmost valence band for certain perpendicular electric field $E_z = 0.022$ V/Å [green line in (a)].

by enhancing the magnitude of the PEF. Although the peak value of the Drude coefficient from the tight-binding model shown in Fig. 4(a) is bigger than that from the multiband $\mathbf{k} \cdot \mathbf{p}$ model shown in Fig. 3(a), the shape of the Drude coefficient curve calculated by both models are similar. Hence we confirm that large Rashba SOC can induce a sign change for the Drude coefficient D_{xy} .

Besides Rashba coefficient enhancement, the sign change in D_{xy} also occurs as a function of chemical potential μ . For a certain Rashba coefficient $\alpha = 0.01$ eV Å ($E_z = 0.022$ V/Å), D_{xy} change its sign from negative to positive by shifting μ below the valence band maxima about 5 meV as shown by the green solid line in Fig. 4(a). When chemical potential μ is near μ_b , the upper spin-split branch of the anisotropic topmost valence band gives rise to six small Fermi circles [blue arrows shown in Fig. 4(b)]. However, the six small Fermi circles merged into two big Fermi circles with counterclockwise spin orientation [as shown by blue arrows in Fig. 4(c)] when the chemical potential μ drops to μ_c . When μ drops to $\mu = \mu_d$, the lower spin-split branch begins to contribute and gives one Fermi circles with six holes and clockwise spin orientations [red arrows in Fig. 4(d)]. When μ goes to $\mu = \mu_e$, the lower spin-split branch gives two concentric circles with the same, clockwise spin orientation (red arrows) and the upper spin-split branch gives two concentric circles with the

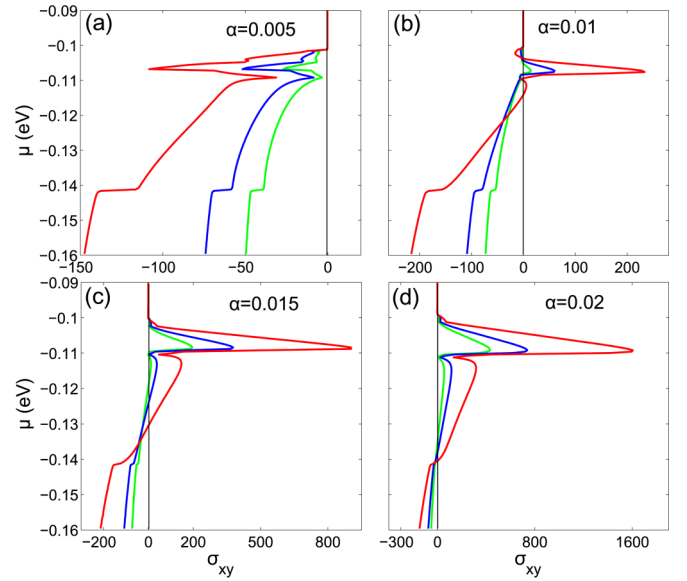


FIG. 5. Charge-spin conductivity σ_{xy} of the InSe monolayer calculated by using the multiband $\mathbf{k} \cdot \mathbf{p}$ model for different Rashba coefficients (a) $\alpha = 0.005$ eV Å, (b) $\alpha = 0.01$ eV Å, (c) $\alpha = 0.015$ eV Å, and (d) $\alpha = 0.02$ eV Å and for different disorder strengths $n_i v_0^2 = 0.4 \times 10^{-3}$ (eV Å)² (red lines), $n_i v_0^2 = 0.8 \times 10^{-3}$ (eV Å)² (blue lines), and $n_i v_0^2 = 1.2 \times 10^{-3}$ (eV Å)² (green lines).

counterclockwise spin orientation (blue arrows), as shown in Fig. 4(e). From $\mu = \mu_b$ to $\mu = \mu_e$, the Lifshitz transition occurs three times and it leads to sign change as a function of chemical potential μ .

B. Disorder effects

In this section, we study the disorder effects on C-S conductivity. For a disordered system, $G^{R(A)}$ in Eq. (4) should be understood as disorder-averaged Green's functions:

$$G^{R(A)} = \frac{1}{\mu - \mathbf{H}^{\text{tot}} \pm i\Gamma}, \quad (6)$$

where $\Gamma = \hbar/(2\tau)$ is the level broadening due to the disorder. For randomly distributed short-range impurities described by a random potential $V(r)$ with Gaussian correlation $\langle V(r)V(r') \rangle = n_i v_0^2 \delta(r - r')$, we can use the Born approximation to obtain $\Gamma = n_i v_0^2 N(\mu)$, where n_i is the impurity density, v_0 is the disorder scattering potential, and $N(\mu)$ is the density of states (DOS) at the chemical potential μ .

By using Eq. (4), we calculate the zero-temperature C-S conductivity vs chemical potential μ for different Rashba coefficients $\alpha = 0.005, 0.01, 0.015, 0.02$ eV Å and plot the results in Figs. 5(a)–5(d). Compared with the Drude coefficient shown in Fig. 3(a), the C-S conductivity shown in Fig. 5 exhibits three new characteristics. First, when the disorder strength $n_i v_0^2$ increases, the level broadening also increases, so the C-S conductivity decreases monotonically. Second, when the chemical potential lies near the valence band maxima, the C-S conductivity is positive for $\alpha = 0.015$ eV Å, which is different from the clean limit case [shown in Fig. 3(a) by the black solid line], where the Drude coefficient has a negative sign. This result indicates that the E_z induced sign change

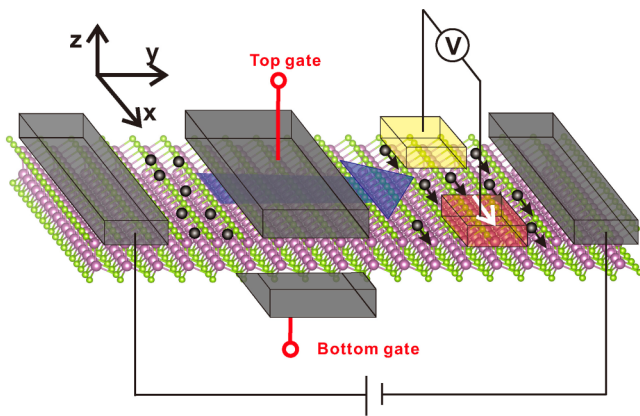


FIG. 6. Sketch of the spin potentiometric measurements device. The Ti/Au contacts are deposited on the left and right edges of the InSe monolayer. The top and bottom gates in this device are used to produce a perpendicular electric field (PEF). The PEF will induce a spin polarization for the charge carrier across this area and the polarization will be detected by the two parallel rows of collinear detector contacts. The red row is ferromagnetic (Fe) and the yellow row is a nonmagnetic reference (Ti/Au). The magnetization direction of the red row, which can be tuned by the in-plane magnetic field, is indicated by the white arrow.

is robust against disorder. To some extent, the disorder can uphold the sign change of the C-S conductivity.

In practice, we can obtain a large Rashba coefficient and observe the sign change by using spin potentiometric measurements, where the projection of the current-generated spin onto the magnetization of a ferromagnetic/tunnel barrier detector contact was measured as a voltage. As shown in Fig. 6, when an unpolarized current flows between the two outer Ti/Au contacts, a spin polarization is produced in the InSe monolayer by the RSOC generated by the gate voltage difference between the top and the bottom gate. Meanwhile, a voltage is measured between the pairs of ferromagnetic (red) detector and the corresponding nonmagnetic Au/Ti (yellow) reference contacts shown in Fig. 6. The projection of this spin polarization onto the magnetization (direction shown by the white arrow) of the ferromagnetic detector contact is recorded as a voltage, with a positive value for the parallel situation shown in Fig. 6. However, the CISP changes sign with increasing the PEF (generated by the gate voltage difference), resulting in a change in sign and magnitude of the detector voltage.

IV. CONCLUSION

We propose and study the current-induced spin polarization in monolayer InSe, which possess unique band structures, based on the 14 band $\mathbf{k} \cdot \mathbf{p}$ Hamiltonian developed by us using the invariant theory. Interestingly, the interplay between the RSOC and unique Mexican hat dispersion at the topmost of the valence band gives rise to many Lifshitz transition points. The in-plane spin polarization would reverse its direction with increasing the perpendicular electric field. This unique feature induced by Rashba SOC is robust against the disorder and it can be detected by the designed spin potentiometric

device. These findings may pave the way for the application of monolayer InSe in 2D spintronic devices.

ACKNOWLEDGMENTS

This work is supported by the Strategic Priority Research Program of the Chinese Academy of Sciences (Grant No. XDB28000000), the NSFC (Grants No. 11434010, No. 61674145, and No. 11574303), the MOST of China (Grants No. 2016YFE0110000 and No. 2017YFA0303400), the Chinese Academy of Sciences (Grants No. QYZDJ-SSW-SYS001 and No. XXH13506-202) and the National Natural Science Foundation of China (NSFC) Grant No. 11774021, and the NSAF grant in NSFC with Grant No. U1930402.

APPENDIX

1. Detailed information of the first-principle calculations

To obtain the monolayer InSe band structure, we use the Vienna *ab initio* simulation package (VASP) [26] within the local density approximation (LDA) [27] and the projector augmented-wave (PAW) [28] pseudopotential. We set the kinetic energy cutoff to 600 eV for the wave function expansion and the k -point grid is sampled by sums over $12 \times 12 \times 1$. The electronic self-consistent calculations converge up to a precision of 10^{-8} eV in total energy difference. A slab model, together with a vacuum layer larger than 20 Å, is employed. The calculated lattice parameters of the monolayer InSe are $a = 5.407$ Å, $d_{\text{In}} = 2.816$ Å, and $d_{\text{Se}} = 5.298$ Å. Our numerical results shows that the energy band gap is 1.461 eV, in good agreement with the previous works [4,29].

Since the spin splitting band structure of monolayer InSe is induced by the Dresselhaus spin-orbit coupling, we determine the Dresselhaus coefficient λ_D by comparing the spin splitting energy calculated by the $\mathbf{k} \cdot \mathbf{p}$ model including the SOC with the splitting energy obtained from first principles calculations along the $\Gamma \rightarrow K$ direction, as shown in Fig. 7.

2. Tight-binding calculations

For the InSe monolayer, the tight-binding Hamiltonian including the SOC is to be developed in this Appendix. In 2016, a 16×16 atomic orbital basis TB Hamiltonian \mathbf{H}_{TB}

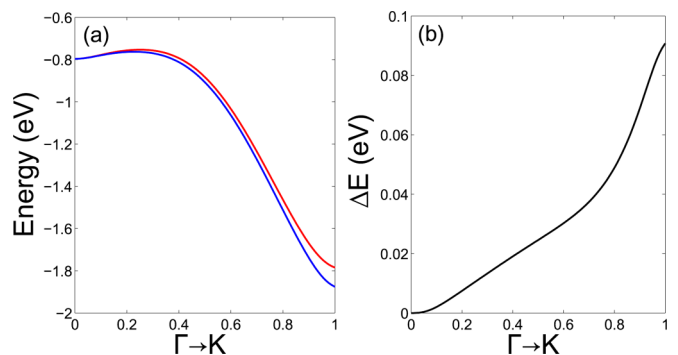


FIG. 7. (a) Topmost valence band structure along $\Gamma \rightarrow K$ direction calculated by density functional theory including SOC. (b) Spin splitting along $\Gamma \rightarrow K$ direction corresponds to (a).

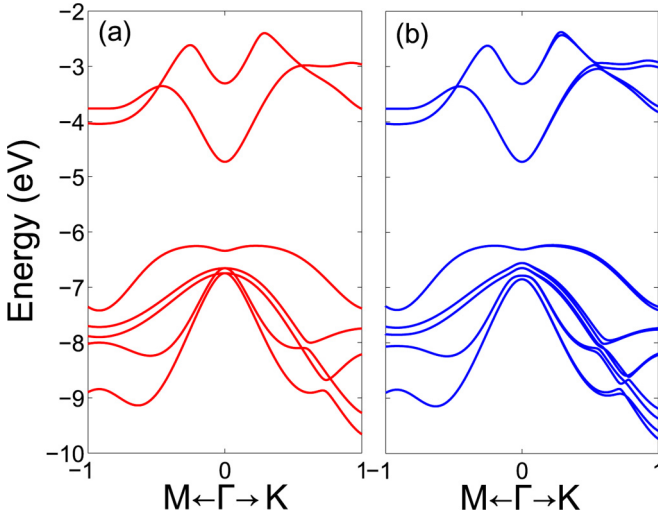


FIG. 8. Band structure from the tight-binding model (a) without and (b) with the SOC.

was constructed [4], and the band structure calculated by this model without the SOC is shown in Fig. 8(a). We can expand this TB Hamiltonian into a 32×32 atomic orbital space with spin. The new Hamiltonian can be developed as $\mathbf{H}_{\text{TB}}^{\text{ASO}} = \mathbf{H}_{\text{TB}} + \mathbf{H}^{\text{ASO}}$, where \mathbf{H}^{ASO} stands for the SOC Hamiltonian stemming from on-site atomic spin-orbit coupling. Generally speaking, the SOC appears as an additional term in the Schrödinger equation given by

$$\hat{H}_{\text{SO}} = \frac{1}{2m^2c^2}(\vec{\nabla}V \times \vec{p}) \cdot \vec{S}, \quad (\text{A1})$$

where m stands for free electron mass, c is the light speed, \vec{p} is the canonical momentum, and $\vec{S} = \hbar/2\vec{\sigma}$ is the spin operator. The potential gradient $\vec{\nabla}V$ can be seen as an electric field. Under the atomic orbital representation, this SOC operator can be rewritten as a term that couples the spin and the angular momentum:

$$\hat{H}_{\text{SO}} = \xi_{\alpha}\vec{L} \cdot \vec{S} = \xi_{\alpha}(L_xS_x + L_yS_y + L_zS_z), \quad (\text{A2})$$

where ξ_{α} is the parameter determined by the atomic radial wave function. We only take the sp orbitals into account in our atomic tight-binding Hamiltonian; therefore, the parameters ξ_{α} depends only upon atoms ξ_{In} , ξ_{Se} . Since the SOC has its largest effect on electrons at the nucleus, the hopping matrix elements of the SOC Hamiltonian between different atoms are assumed to be zero. Therefore, the SOC Hamiltonian under the atomic orbit representation has a diagonal block form.

The InSe monolayer has mirror symmetry, so the basis has definite parity along z axis; therefore, we can

reduce the system to two 8×8 matrices without taking the spin-orbit coupling into consideration. The first 8×8 matrix can be constructed in the even parity representation $\{|M_s^+\rangle, |M_x^+\rangle, |M_y^+\rangle, |M_z^+\rangle, |X_s^+\rangle, |X_x^+\rangle, |X_y^+\rangle, |X_z^+\rangle\}$ and the other 8×8 matrix can be constructed in the odd parity representation $\{|M_s^-\rangle, |M_x^-\rangle, |M_y^-\rangle, |M_z^-\rangle, |X_s^-\rangle, |X_x^-\rangle, |X_y^-\rangle, |X_z^-\rangle\}$. The TB Hamiltonian matrix elements in this representation have already been developed in Ref. [4]. Here, we further consider the spin-orbit coupling in this representation, and the spin-orbit coupling Hamiltonian can be written as

$$\begin{aligned} \mathbf{H}^{\text{ASO}} &= \begin{bmatrix} \xi_{\text{In}}h_{\text{so}} & 0 & 0 & 0 \\ 0 & \xi_{\text{Se}}h_{\text{so}} & 0 & 0 \\ 0 & 0 & \xi_{\text{In}}h_{\text{so}} & 0 \\ 0 & 0 & 0 & \xi_{\text{Se}}h_{\text{so}} \end{bmatrix} \\ &+ \begin{bmatrix} 0 & 1 \\ 1 & 0 \end{bmatrix} \otimes \begin{bmatrix} \xi_{\text{In}}H_{\text{SO}} & 0 \\ 0 & \xi_{\text{Se}}H_{\text{SO}} \end{bmatrix}, \\ h_{\text{SO}} &= \begin{bmatrix} 0 & 0 & 0 & 0 \\ 0 & 0 & -is_z & 0 \\ 0 & is_z & 0 & 0 \\ 0 & 0 & 0 & 0 \end{bmatrix}, \\ H_{\text{SO}} &= \begin{bmatrix} 0 & 0 & 0 & 0 \\ 0 & 0 & 0 & is_y \\ 0 & 0 & 0 & -is_x \\ 0 & -is_y & is_x & 0 \end{bmatrix}, \end{aligned} \quad (\text{A3})$$

where s_x, s_y, s_z are the Pauli matrices. In our calculation we fit the topmost valence band spin splitting from the tight-binding model with the results from first principle calculations as shown in Fig. 7 and finally get $\xi_{\text{In}} = 0.08$ eV and $\xi_{\text{Se}} = 0.1$ eV. Under the tight-binding model with these two parameters, we can obtain a spin splitting band structure as shown in Fig. 8(b).

Here, we simulate the effect of the perpendicular electric field (E_z) on the band structure of the InSe monolayer by adding the on-site energy. Since we set the xy mirror of the crystal as the zero potential energy point, the E_z dependent Hamiltonian in the above representation can be written as

$$\mathbf{H}_{E_z} = \begin{bmatrix} 0 & 1 \\ 1 & 0 \end{bmatrix} \otimes \begin{bmatrix} \Lambda_{\text{In}}\mathcal{I} & 0 \\ 0 & \Lambda_{\text{Se}}\mathcal{I} \end{bmatrix}, \quad (\text{A4})$$

where \mathcal{I} is the 4×4 identity matrix and $\Lambda_{\text{In}} = E_z d_{\text{InIn}}/2$ ($\Lambda_{\text{Se}} = E_z d_{\text{SeSe}}/2$). E_z is the magnitude of the perpendicular electric field. The total tight-binding Hamiltonian can be written as

$$\mathbf{H}_{\text{TB}}^{\text{tot}} = \mathbf{H}_{\text{TB}} + \mathbf{H}^{\text{ASO}} + \mathbf{H}_{E_z}. \quad (\text{A5})$$

- [1] V. Zólyomi, N. D. Drummond, and V. I. Fal'ko, *Phys. Rev. B* **87**, 195403 (2013).
 [2] D. V. Rybkovskiy, A. V. Osadchy, and E. D. Obraztsova, *Phys. Rev. B* **90**, 235302 (2014).
 [3] P. Li and I. Appelbaum, *Phys. Rev. B* **92**, 195129 (2015).

- [4] S. J. Magorrian, V. Zólyomi, and V. I. Fal'ko, *Phys. Rev. B* **94**, 245431 (2016).
 [5] T. Cao, Z. Li, and S. G. Louie, *Phys. Rev. Lett.* **114**, 236602 (2015).
 [6] S. Lei, L. Ge, Z. Liu, S. Najmaei, G. Shi, G. You, J. Lou, R. Vajtai, and P. M. Ajayan, *Nano Lett.* **13**, 2777 (2013).

- [7] D. A. Bandurin, A. V. Tyurnina, G. L. Yu, A. Mishchenko, V. Zolyomi, S. V. Morozov, R. K. Kumar, R. V. Gorbachev, Z. R. Kudrynskiy, S. Pezzini, Z. D. Kovalyuk, U. Zeitler, K. S. Novoselov, A. Patane, L. Eaves, I. V. Grigorieva, V. I. Fal'ko, A. K. Geim, and Y. Cao, *Nat. Nanotechnol.* **12**, 223 (2017).
- [8] M. Zhou, R. Zhang, J. Sun, W.-K. Lou, D. Zhang, W. Yang, and K. Chang, *Phys. Rev. B* **96**, 155430 (2017).
- [9] V. M. Edelstein, *Solid State Commun.* **73**, 233 (1990).
- [10] C. Huang, M. Millettari, and M. A. Cazalilla, *Phys. Rev. B* **96**, 205305 (2017).
- [11] H. J. Zhang, S. Yamamoto, B. Gu, H. Li, M. Maekawa, Y. Fukaya, and A. Kawasuso, *Phys. Rev. Lett.* **114**, 166602 (2015).
- [12] A. Manchon, H. C. Koo, J. Nitta, S. M. Frolov, and R. A. Duine, *Nat. Mater.* **14**, 871 (2015).
- [13] C. H. Li, O. M. J. van 't Erve, S. Rajput, L. Li, and B. T. Jonker, *Nat. Commun.* **7**, 13518 (2016).
- [14] C. H. Li, O. M. J. van 't Erve, J. T. Robinson, Y. Liu, L. Li, and B. T. Jonker, *Nat. Nanotechnol.* **9**, 218 (2014).
- [15] M. Trushin and J. Schliemann, *Phys. Rev. B* **75**, 155323 (2007).
- [16] M. Duckheim, D. Loss, M. Scheid, K. Richter, I. Adagideli, and P. Jacquod, *Phys. Rev. B* **81**, 085303 (2010).
- [17] A. Dyrdał, J. Barnaś, and V. K. Dugaev, *Phys. Rev. B* **89**, 075422 (2014).
- [18] A. Dyrdał and J. Barnaś, *Phys. Rev. B* **92**, 165404 (2015).
- [19] M. Offidani, M. Millettari, R. Raimondi, and A. Ferreira, *Phys. Rev. Lett.* **119**, 196801 (2017).
- [20] M. Zhou, D. Zhang, S. Yu, Z. Huang, Y. Chen, W. Yang, and K. Chang, *Phys. Rev. B* **99**, 155402 (2019).
- [21] I. Garate and M. Franz, *Phys. Rev. Lett.* **104**, 146802 (2010).
- [22] D. S. Smirnov and L. E. Golub, *Phys. Rev. Lett.* **118**, 116801 (2017).
- [23] G. Seibold, S. Caprara, M. Grilli, and R. Raimondi, *Phys. Rev. Lett.* **119**, 256801 (2017).
- [24] K. Shen, G. Vignale, and R. Raimondi, *Phys. Rev. Lett.* **112**, 096601 (2014).
- [25] E. Lesne, Y. Fu, A. Fert, M. Bibes, and L. Vila, *Nat. Mater.* **15**, 1261 (2016).
- [26] G. Kresse and J. Furthmüller, *Phys. Rev. B* **54**, 11169 (1996).
- [27] W. Kohn and L. J. Sham, *Phys. Rev.* **140**, A1133 (1965).
- [28] P. E. Blöchl, *Phys. Rev. B* **50**, 17953 (1994).
- [29] X. Yang, B. Sa, H. Zhan, and Z. Sun, *J. Mater. Chem. C* **5**, 12228 (2017).